$LiTa_2PO_8$-based Polymer-Ceramic Electrolyte Paved the way to High-Performance Solid-State Lithium Metal Batteries

Asish Kumar Das[a], Manish Badole[a], Hari Narayanan Vasavan[a], Samriddhi Saxena[a], Pratiksha Gami[a],

Neha Dagar[a], Sunil Kumar[a, b] *

a Department of Metallurgical Engineering and Materials Science, Indian Institute of Technology Indore, Simrol, 453552, India

b Center for Electric Vehicle and Intelligent Transport Systems, Indian Institute of Technology Indore, Simrol, 453552, India

* Email: sunil@iiti.ac.in

Abstract:

Solid composite electrolytes, leveraging the advantages of both ceramic and polymers, are emerging as a viable alternative to liquid electrolytes in all-solid-state lithium metal batteries. Here, we have developed a polymer-ceramic composite electrolyte with an area-specific resistance of ~ 94 Ω cm^2 at room temperature (RT) by solution casting method. A Li-ion conducting $LiTa_2PO_8$ ceramic with an RT bulk conductivity of ~ 3.2×10^{-4} S cm^{-1} was synthesized to act as an active filler in a PEO/PVDF-HFP polymer matrix complexed with LiTFSI salt to obtain a polymer-ceramic composite electrolyte. The symmetric lithium cell with the optimized electrolyte exhibited excellent cyclability over 950 cycles at an areal current density of 0.2 mA cm^{-2}. The full cell with $LiFePO_4$ cathode and lithium metal anode delivered a specific capacity of ~ 115 mAh g^{-1} with ~ 85% capacity retention after the 500 cycles at 1C at RT, making it a viable alternative to be adopted in Li-ion batteries for room temperate applications.

Keywords: *All-solid-state batteries; ionic conductivity; composite electrolytes; lithium-ion transference number; active filler.*

1. Introduction

Lithium-ion battery technology has permeated nearly every aspect of modern life, yet its reliance on liquid electrolytes poses significant challenges.[1, 2] The complexity, flammability, and toxicity associated with liquid electrolytes have hindered further advancements in lithium-ion batteries. To overcome these challenges, it has become imperative to explore alternatives. Solid electrolytes present a promising solution, offering the potential to manufacture batteries with enhanced safety and energy density compared to conventional lithium-ion batteries. Solid electrolytes are currently the cornerstone of solid-state battery technology undergoing rapid development.[3]

Solid electrolytes can be categorized into two main types: inorganic solid electrolytes (ISEs) and solid polymer electrolytes (SPEs). ISEs are known for their exceptional thermal stability and high ionic conductivity. Oxide-based ISEs, such as lithium lanthanum titanate ($Li_{0.33}La_{0.557}TiO_3$) and garnet-type materials (e.g., $Li_7La_3Zr_2O_{12}$), have attracted considerable interest due to their high ionic conductivity and excellent chemical stability.[4-12] These materials typically exhibit good compatibility with lithium metal anodes and are promising candidates for solid-state lithium batteries. Sulfide-based solid electrolytes, including materials like $Li_{10}GeP_2S_{12}$ and Li_6PS_5Cl, have emerged as alternatives to oxide-based electrolytes.[13-19] These materials often offer higher ionic conductivity at room temperature than their oxide counterparts. However, chemical stability and compatibility with electrode materials remain key challenges that must be addressed for commercial applications.[20, 21] NASICON-based solid electrolytes, such as $LiZr_2(PO_4)_3$ (LZP) and $LiGe_2(PO_4)_3$ (LGP), are known for their good chemical stability and wider electrochemical stability window.[22, 23] These materials offer the potential for high-voltage cathode materials and can operate at elevated temperatures but are limited by their poor ionic conductivities at room temperature. A major bottleneck in the application of ISE in solid-state batteries stems from their inability to establish effective contact with the electrode. This leads to significant interfacial impedance, which hampers the transfer of lithium ions between the electrolyte and electrodes. Consequently, batteries employing ISEs often suffer reduced capacity, poor rate performance, and shorter cycle life.

Polymers, such as PEO, PEGDME, P(VDF-HFP), etc., are used along with different lithium salts such as Lithium bis(trifluoromethane)sulfonimide (LiTFSI), Lithium difluoro(oxalato)borate (LiDFOB), etc., and are also utilized in solid-state batteries.[24-30] The polymers (except single-ion lithium-ion conducting) are incapable of lithium-ion conduction. The salts added to the polymer get dissociated into Li^+ and the corresponding anions, which enable the polymer to conduct lithium-ions via various mechanisms like polymer chain movement, segmental motion, hopping, etc.[31] The solid electrolyte interphase formation typically depends on the polymer and salt used in composites. In addition, properties like the dissociation energy of salt, the size & mass of the anion, etc., play pivotal roles in determining the electrochemical performance of the battery. Moreover, during in-situ polymerization, the salt can initiate the polymerization process without using any additional initiators. Solid polymer electrolytes (SPEs) offer flexibility and good affinity with electrodes.[32-34] Nevertheless, solid polymer electrolytes (SPEs) face a hurdle due to their low ionic conductivity, typically below 10^{-5} S cm^{-1}. This limitation poses a challenge to their integration into all-solid-state lithium batteries. These challenges emphasize the need for further development and innovation in solid-state electrolytes. These challenges can be addressed by employing various techniques like the addition of inorganic fillers blending, in-situ photo-polymerization, and solvent-free crosslinking. Among these, incorporating inorganic fillers into the polymer matrix to create composite polymer electrolytes emerged as a promising strategy to improve the performance of solid-state lithium metal batteries.[35-37]

These inorganic fillers can be categorized into inert fillers, such as Al_2O_3, TiO_2, SiO_2, and CeO_2, and active fillers, including perovskite-type, garnet-type, and NASICON-type materials.[38-42] Inert fillers play a crucial role as plasticizers by increasing the amorphousity of the polymer matrix. This facilitates the dissociation of salt through Lewis acid-base interactions.[43] On the other hand, active fillers offer dual benefits: augmentation of lithium-ion (Li^+) mobility by facilitating the segmental movement of the polymer chain, like inert fillers, and promote rapid Li^+ transport within the ceramic phase. This dual action creates efficient pathways for Li^+ conduction at the interface between the polymer and the ceramic filler, resulting in remarkable synergistic effects. In 2018, Kim et al. systematically explored corner-sharing polyanionic phases with $Li_x(MO_{6/2})_m(TO_{4/2})_n$ configurations, where M and T represent octahedral and tetrahedral cation sites, respectively.[44, 45] Through rigorous search, they unveiled monoclinic $LiTa_2PO_8$, denoted as $Li_x(TaO_{6/2})_2(PO_{4/2})_1$ or LTPO, as a novel type of highly efficient Li-ion conducting oxide. The room temperature (25 °C) bulk lithium-ion conductivity of LTPO is reported to be around 10^{-4} S cm^{-1}.[44] High Li+ conductivity makes LTPO an attractive candidate for solid electrolyte application in lithium batteries. Unfortunately, LTPO is also reported to be chemically unstable with lithium metal, forming a highly resistive passivating layer that limits its application as a ceramic electrolyte.[45]

In the current study, powders of $LiTa_2PO_8$ (LTPO) are used as active fillers in a PEO-P(VDF-HFP)-LiTFSI salted polymer matrix to create a composite solid electrolyte. The LTPO demonstrates bulk conductivity on the order of ~10^{-4} S cm^{-1}. In PEO-P(VDF-HFP) polymer, P(VDF-HFP) provides mechanical stability, whereas PEO is highly chemically stable with lithium metal. LiTFSI emerges as the appropriate salt due to its robust complexation with PEO-P(VDF-HFP) and ability to curtail anionic mobility, attributed to the sizable and weighty $TFSI^-$ ion. The addition of LTPO enhances the ionic conductivity of the modified polymer electrolyte by providing additional lithium-ion transport pathways. The study reports on the electrochemical performance of solid-state symmetric lithium cells and full cells ($LiFePO_4$ as the cathode) utilizing the composite solid electrolyte with different percentages of the ceramic content.

2. Experimental method

2.1 LTPO synthesis

Stoichiometric amounts of lithium carbonate (Li_2CO_3), Tantalum pentoxide (Ta_2O_5), and ammonium dihydrogen phosphate ($NH_4 \cdot H_2PO_4$) raw materials were measured. To compensate for the evaporation of Li_2O at high temperatures, 10 wt.% of excess Li_2CO_3 was added. The mixture underwent ball milling for 12 h, then heated at 600 °C for 12 h to facilitate thermal decomposition. Subsequently, the obtained powders were ball milled again for 12 h and then dried. The resulting powders were added to a die and pressed into ceramic pellets of 10 mm diameter under a uniaxial pressure of ~ 200 MPa. Finally, the green ceramic pellets were reactive sintered at 1150 °C for 12 h.

2.2 Composite solid electrolyte preparation

Composite solid-state electrolytes were fabricated using the solvent-casting technique. Initially, PEO and P(VDF-HFP) (1:1 wt. ratio) were dissolved in a mixed solvent of acetonitrile and DMF, followed by stirring for 3 h. LiTFSI salt was added to the polymeric solution at a 60 wt.% polymer concentration. Subsequently, LTPO ceramic particles synthesized at 1150 °C were introduced into the solution and stirred at 400 rpm for 24 h, with different weight fractions of ceramics to salt-polymer PEO-P(VDF-HFP)-LiTFSI, to achieve a homogeneous solution. This solution was cast onto a PTFE plate and dried at 50 ℃ for 24 h in a vacuum oven to eliminate the solvent. The resulting dried LTPO*x* (*x* = wt. percentage of ceramics in the composite solid electrolyte) was subsequently cut into 18 mm round pieces and stored in a glove box filled with Argon.

2.3 Coin cell fabrication

The symmetric lithium cells named Li|LTPO*x*|Li cells were fabricated with lithium metal as the electrodes and LTPO*x* electrolyte membranes as the electrolyte. The asymmetric Li|LTPO*x*|SS cell configuration was fabricated with lithium metal as the anode and SS (stainless steel) as the working electrode to measure the electrochemical stability window of the LTPO*x* solid electrolytes. For a full cell Li|LTPOx|$LiFePO_4$ cell fabrication, $LiFePO_4$ cathode slurry was prepared with a weight ratio of PVDF: Ketjen black: active material ($LiFePO_4$) as 15: 10: 75. Al current collector was used for cathode slurry coating with an areal active material density of 1.5 mg cm^{-2}.

2.4 Characterization techniques

Various analytical techniques were employed to characterize the phase composition and properties of ceramic $LiTa_2PO_8$ (LTPO), polymer-salt complexes, and composite solid electrolyte (LTPO*x*) membranes. X-ray diffraction (XRD) analysis was conducted using an Empyrean X-ray diffractometer with Cu-Kα radiation covering the 2θ range of 10° to 60°. Rietveld refinement was used for obtaining the crystallographic parameters from the XRD data (employing the TOPAS academic version 6 software).[46] The microstructural characteristics of the prepared samples were investigated using a JEOL-7610+ field emission scanning electron microscope (FE-SEM). FTIR spectra were obtained using a PerkinElmer Spectrum IR (Model number: Spectrum 2) spanning a 500 – 1800 cm^{-1} range. impedance data were obtained utilizing an NF Corp. LCR meter (Model: ZM2376) and at an applied 10 mV input signal in 1 Hz - 1 MHz range on sintered LTPO pellets with silver electrodes painted on either side, as well as the lithium symmetric cells Li|LTPO*x*|Li. DC polarisation tests were carried out in Li|LTPO*x*|Li cells, along with linear sweep voltammetry (LSV) in asymmetric Li|LTPO*x*|SS (stainless-steel) cells using a Keithley Source Meter Unit (model 2450-EC). Linear sweep voltammetry tests were carried out in the 2.5-6.0 V range at scan rate of 0.1 mV s^{-1} at 25 °C. Galvanostatic charge-discharge (GCD) measurements were also carried out on Li|LTPO20|Li cells and Li|LTPO20|$LiFePO_4$ cells with the help of a Neware CT-2001A battery tester. The electrochemical experiments were performed at room temperature.

3. Results and discussion

3.1 X-ray diffraction analysis

Figure 1(a) presents the X-ray diffraction (XRD) pattern of $LiTa_2PO_8$ (LTPO) reactive sintered at 1150 °C for 12 h with a heating rate of 5 °C min^{-1}.

The Rietveld refinement performed using TOPAS software (academic version) confirmed a monoclinic phase (space group: *C*2/*c*) with lattice parameters a = 9.7196(2) Å, b = 11.5424(3) Å, c = 10.7036(3) Å, β = 90.025(3) and V = 1200.81(5) $Å^3$.[46] During refinement (the refinement results are provided in Table S1), the monoclinic structure was taken as the starting model with

Wyckoff positions determined by Adams and Co., and. and the generated CIF file was employed to investigate the lithium-ion kinetics in the crystal structure.[45]

Figures 1(b) and 1(c) show the possible lithium-ion migration pathway along with the lithium-ion migration barrier energy between two adjacent lithium sites inside the $LiTa_2PO_8$ monoclinic crystal structure, generated with the help of softBV software using a grid resolution of 0.1 Å.[47-49] The one-dimensional lithium-ion conduction occurs via Li2 and Li4 sites with an energy barrier of 0.186 eV, while three-dimensional lithium-ion conduction pathways occur through Li2-Li3 sites with an energy barrier of 0.251 eV. The facile lithium migration pathway provided by the crystal structure could boost the lithium-ion conductivity of the sample. Figure S1 compares the XRD patterns of the LTPO20 composite solid electrolyte and $LiTa_2PO_8$ ceramic (only the LTPO20 sample's xrd is shown as a representative, as there was no discernible change in xrd patterns of LTPO10, LTPO20, and LTPO30). The presence of high-intensity XRD peaks of $LiTa_2PO_8$ in the former suggests the successful incorporation of LTPO ceramics in the PEO-(PVDF-HFP)-LiTFSI polymeric salt matrix.

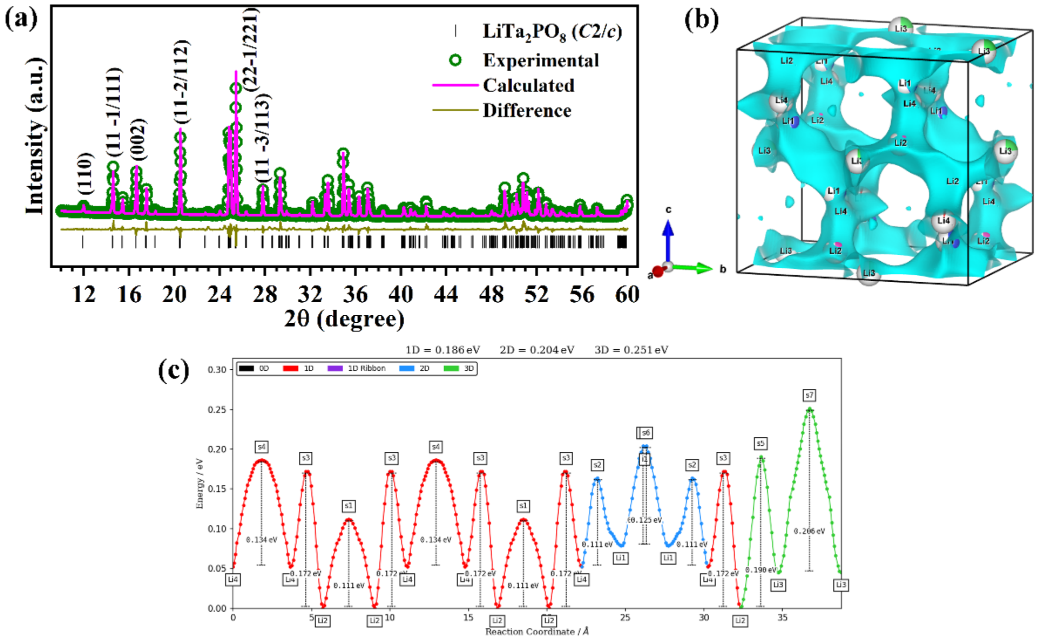

Figure 1: (a) Room temperature powder XRD data (open green symbols) for LiTa$_2$PO$_8$ (LTPO) sample calcined at 1150 °C for 12 h. The calculated pattern is depicted as a thick magenta line; the profile difference is shown by a yellow line. The Bragg positions for LTPO are indicated by black vertical bars. (b) The lithium-ion migration pathway in the monoclinic LiTa$_2$PO$_8$ (C2/c) crystal was generated using softBV software. (c) The energy difference at different lithium sites in the LiTa$_2$PO$_8$ crystal structure using softBV software.

3.2 Microstructure analysis

The scanning electron microscopy image of the reactive sintered LiTa$_2$PO$_8$ pellet's surface (relative density of ~ 93%), along with the elemental distribution of Ta, P, and O, are shown in Figure 2(a) inset and Figures 2(b-d), respectively. Figure 3(a-e) illustrates the energy dispersive spectroscopy (EDS) maps of the LTPO20 solid electrolyte sample. The elemental distribution of N and S indicates the LiTFSI salt in the polymer matrix. Further, the uniform distribution of LTPO ceramic fillers is confirmed by the elemental distribution of Ta, P, and O. The well-connected polymer chains in LTPO20 can foster the lithium-ion percolation with better Li$^+$ transport properties as compared to the LTPO0 (PEO-P(VDF-HFP)-LiTFSI) electrolyte with no ceramic fillers, by providing extra lithium-ion conduction pathways.

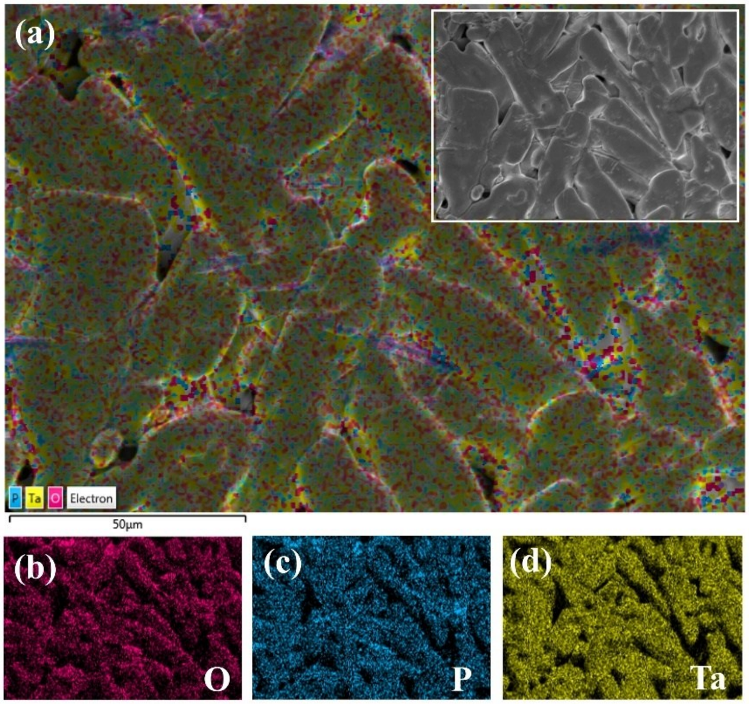

Figure 2: (a)EDS mapping of sintered $LiTa_2PO_8$ pellet along with SEM image as inset. (b-d) Elemental distributions of O, P, and Ta.

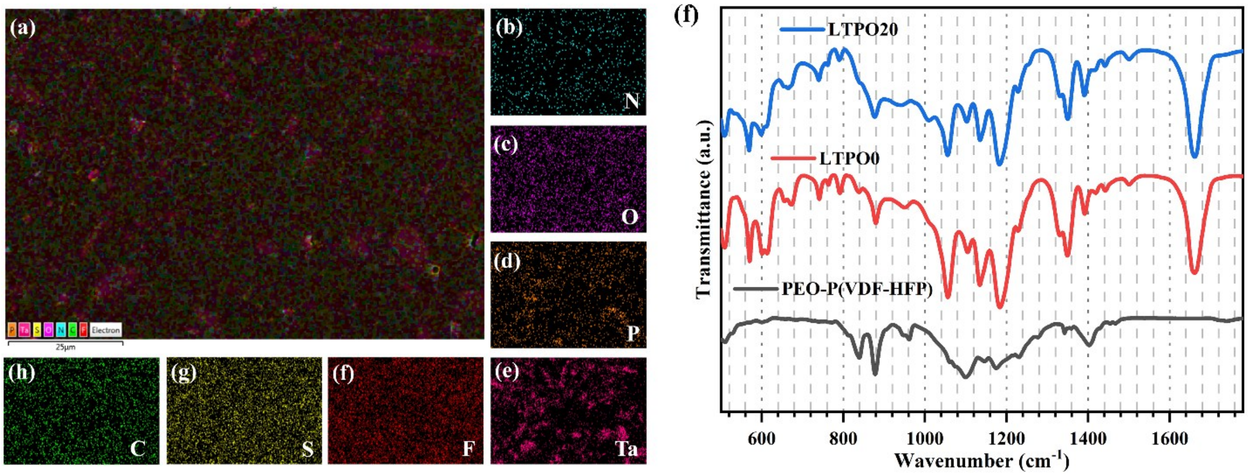

Figure 3: (a)EDS mapping of sintered $LiTa_2PO_8$ pellet along with SEM image as inset. (b-e) Elemental distributions of N, O, P, Ta, F, S, and C. (f) FTIR spectra of PEO-P(VDF-HFP), LTPO0, and LTPO20.

3.3 FTIR analysis

Figure 3(b) illustrates the FTIR spectra, revealing changes in absorbance within the range of 500 cm^{-1} to 1780 cm^{-1} following the addition of salt and ceramic filler. In the PEO-P(VDF-HFP) polymer matrix, peaks observed at approximately 840, 878, 1174, 1278, and 1402 cm^{-1} correspond to the mixed mode of molecular vibrations, including -CH2 rocking, combined -C-C vibrations, -CF2 symmetric stretching, C-F symmetric stretching, -CF3 symmetric stretching, and -CH2 wagging, respectively.[50-52] Additionally, the appearance of doublet peaks at ~1340 cm^{-1} and 1360 cm^{-1} signifies -CH2 wagging of PEO polymer, whereas peaks around ~1058 cm^{-1} represent C-O-C stretching of PEO.[53] Further distinctive vibrations associated with PEO and P(VDF-HFP) remain evident both before and after the introduction of Li-salt and LTPO ceramic filler. Observations in the FTIR spectrum of LTPO0 revealed additional peaks at approximately 1661, 1502, and 571 cm^{-1} in the LTPO0. The appearance of the peak at 571 cm^{-1} is attributed to asymmetric -CF3 bending vibrations of LiTFSI.[52] Peaks at ~ 765 cm^{-1} and ~ 740 cm^{-1} in the FTIR spectra of both LTPO0 and LTPO20 denote Li^{+}-$TFSI^{-}$ contact pairs and free $TFSI^{-}$, respectively.[54] [55] Notably, LTPO fillers act as Lewis acid sites affecting the molecular bonds (-SO_2- chain) in $TFSI^{-}$. This causes a slight peak shift in the FTIR spectra of the polymer-salt matrix upon incorporation of ceramic fillers. Such changes, attributed to the occurrence of Lewis acid-base interactions between the ceramic particles and $TFSI^{-}$, have been reported in the literature.[56]

3.4 Complex impedance analysis

The impedance measurements for the LTPO pellet (silver electrodes were painted on the flat surfaces) and LTPO*x* (the composite membranes were placed between two stainless steel spacers) were carried out in the frequency range of 1 Hz – 1 MHz using a 10 mV perturbation potential. Figure 4(a) presents the Nyquist plot of the LTPO sample at room temperature, and the corresponding equivalent circuit used to model the data is shown in Figure 4(a) inset. The straight-line feature in the low-frequency region denotes the non-ionic-conducting nature of the silver electrodes. CPE1||R_g presents the grain component, whereas CPE2||R_{gb} denotes the grain-boundary component. Utilizing the values of R_g (from fitting) alongside the dimensions of the sample, the room temperature bulk conductivity of LTPO was determined to be ~ 3.2×10^{-4} S cm^{-1}. The application of LTPO pellets in solid-state batteries is hindered due to the presence of highly resistive grain boundaries and the chemical instability of the LTPO ceramic with lithium metal. Further, the activation energy bulk conduction of the LTPO sample was calculated to be ~ 0.285 ± 0.006 eV using the Arrhenius equation:

$$\sigma(T) = \sigma_0 e^{-\frac{Ea}{k_B T}} \tag{1}$$

where T denotes the absolute temperature in Kelvin, σ_0 and E_a represent the pre-exponential factor and activation energy, respectively (Figure 4(b)).

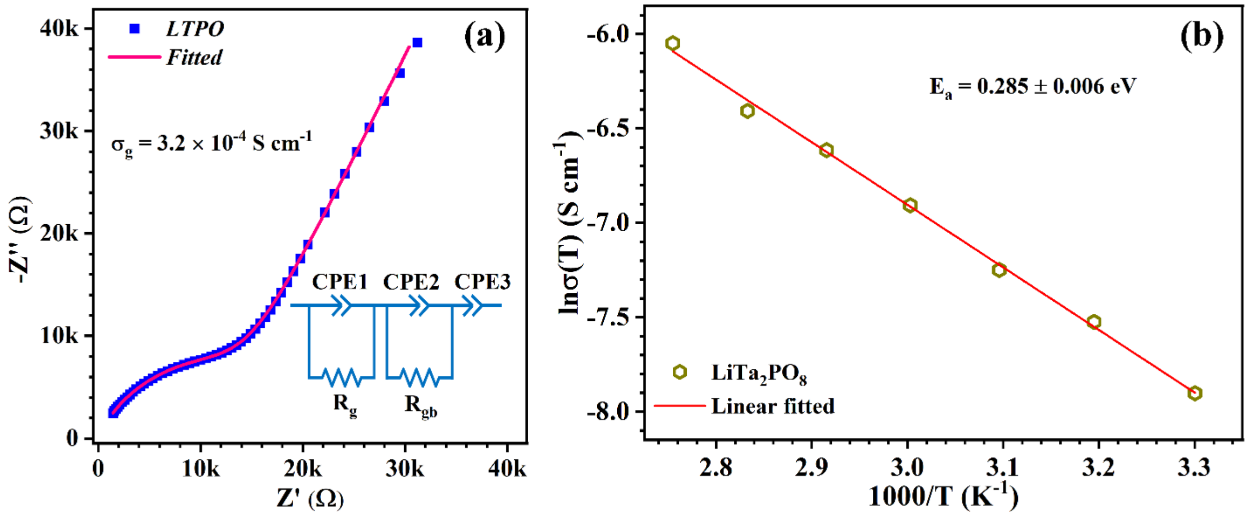

Figure 4: (a) Nyquist plot of $LiTa_2PO_8$ (inset displays the equivalent circuit used for fitting the impedance data) at room temperature. The scattered symbol and the pink line represent the experimental and fitted data, respectively. (b) Linear fitting of temperature-dependent conductivities of $LiTa_2PO_8$ sample using the Arrhenius equation.

In the Nyquist plot at room temperature for LTPO20 (Figure 5(a)) (the Nyquist plots of LTPO0, LTPO10 (10 wt.% LTPO ceramics in composite), and LTPO30 (30 wt.% LTPO ceramics in composite) electrolytes are presented as Figures S2, S3, and S4, respectively in Supplementary Information), a tail feature (CPE2) in the low-frequency region signifies the ion-blocking characteristic associated with the stainless steel. A partial semicircular arc (modeled by R||CPE1) observed in the high-frequency range represents the lithium-ion movement within the composite electrolyte. The determined 'R' values from the fitting, thickness, and surface area were employed to calculate conductivity values for the composite electrolyte samples. Table 1 presents the conductivity (at RT) and activation energy (determined from the linear fitting shown in Figure 5(b), using equation 1) of the composite solid electrolytes LTPO*x*. An increase in conductivity and a decrease in the activation energy was observed as a result of incorporating the ceramic powders in the polymer matrix. The LTPO20 sample, with conductivity of ~ 0.9×10^{-4} S cm^{-1} at room temperature and activation energy of ~ 0.25 eV, outperformed the other compositions in conductivity and activation energy. It is known that incorporating lithium-ion conducting ceramic powders in polymers diminishes the semi-crystalline nature of the polymer matrix and provides additional conduction channels through the ceramic grains or space-charge regions present at the ceramic-polymer interface, thereby enhancing lithium-ion conduction.[57, 58] It may be noted that the DMF solvent can't be removed from the polymer matrix completely at 50 °C, even under vacuum, as confirmed by recent studies where residual DMF forms complexes with Li^+ and facilitates ionic conductivity.[59-61] The lower conductivity and higher activation energy of LTPO30 compared to the LTPO20 sample could be due to the agglomeration of LTPO ceramic fillers.

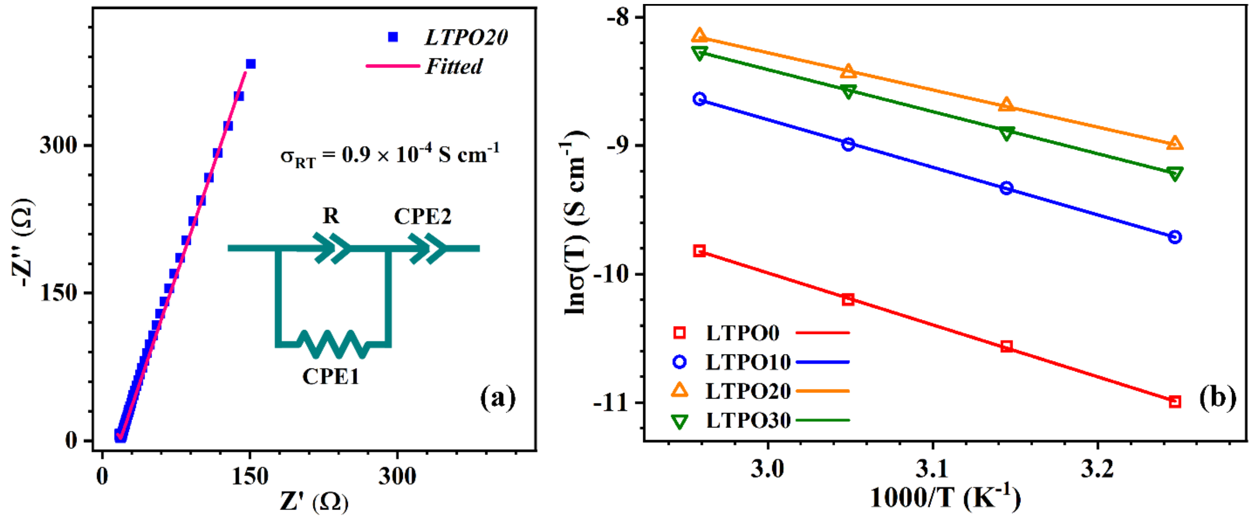

Figure 5: (a) Nyquist plot of LTPO20 electrolyte sample (inset displays the equivalent circuit used to fit the impedance data) at room temperature. The scattered symbol and the pink line represent the experimental and fitted data, respectively. (b) Linear fitting of conductivities of LTPOx at different temperatures using the Arrhenius equation.

Table 1: *RT conductivity (σ_{RT}) and activation energy (E_a) values obtained for various samples (LTPOx).*

Sample	**σ_{RT} (S cm^{-1})**	**E_a (eV)**
LTPO0	1.3×10^{-5}	0.348 ± 0.005
LTPO10	5.6×10^{-5}	0.319 ± 0.004
LTPO20	9.2×10^{-5}	0.249 ± 0.005
LTPO30	7.5×10^{-5}	0.282 ± 0.004

3.5 Li^+ transference number

The Bruce-Vincent method was used to probe the Li^+ transference number in the electrolyte sample.[62] This technique integrates direct current (DC) and alternating current (AC) measurement methods. In this study, to measure the Li^+ transference number, a 0.05 V DC potential (ΔV) is applied to Li|LTPO*x*|Li cells for 3 h. The impedance of the symmetric cell is measured before applying DC potential and upon the removal of DC potential using a 10 mV AC perturbation to determine the interfacial resistance of the cell. Under the DC potential, both cationic and anionic species contribute to the initial current value (I_0) at t = 0 h. However, over time, there is a decline in the current value due to a reduction of the anionic current as the anions are blocked at the lithium metal electrode's surface, and a counter-electric field develops in the direction opposite of the applied DC field. At a steady state (t = 3 h), the current (Iss) is solely due to the migration of the cationic species through the electrolyte. In Figure 6(a), the current variation in Li|LTPO20|Li cells under a 50 mV DC potential over 3 h is depicted.

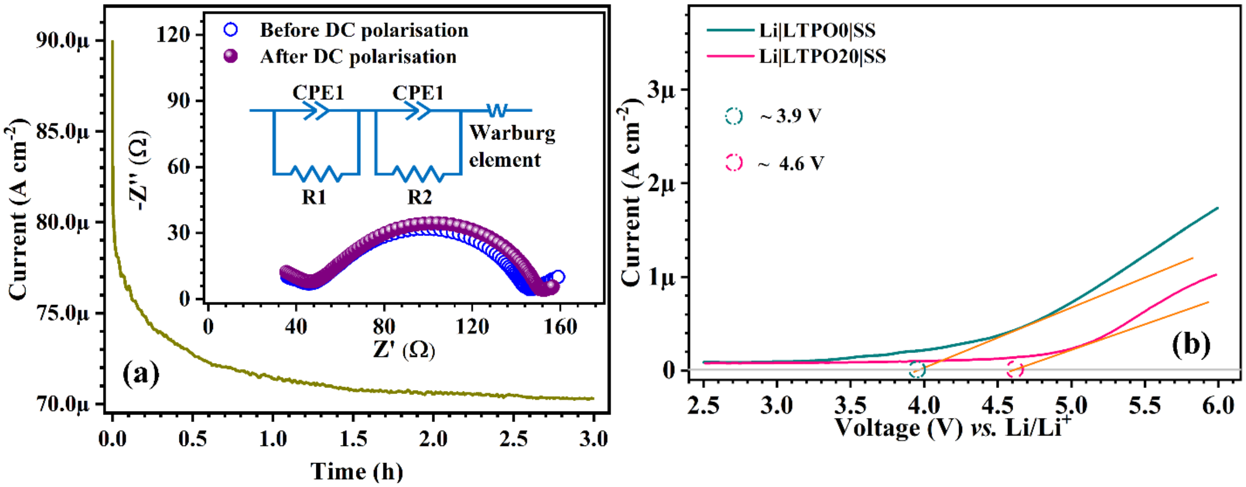

Figure 6: (a) Change in current with time under 50 mV DC bias load on Li|LTPO20|Li cell at room temperature. The inset shows the Nyquist plots at t = 0 h & t = 3 h with the appropriate equivalent circuit employed to fit the data. (b) Linear sweep voltammetry curves of Li|LTPO0|SS cell and Li|LTPO20|SS cell at a scan rate of 0.1 mV s^{-1} *at room temperature.*

The inset displays Nyquist plots of Li|LTPO20|Li cells measured at t = 0 h and t = 3 h. The impedance data was analyzed with the help of an equivalent circuit model (Figure 6(a) inset). The composite electrolyte and symmetric cell's total DC resistance are indicated by the high-frequency and low-frequency intercepts of the semi-circular arcs, respectively. A very low ~ 7 Ω change is observed in the interfacial resistance. In contrast, there was no significant change in the composite electrolyte's bulk resistance, suggesting the composite electrolyte's chemical stability with lithium metal. The lithium-ion transference values for LTPO*x* were calculated using equation (2) and are given in Table S2.

$$t_{Li^+} = \frac{I_{ss}(\Delta V - I_0 R_0)}{I_0(\Delta V - I_{ss} R_{ss})} \tag{2}$$

In liquid electrolytes, there is always a trade-off between ionic conductivity and lithium-ion transference number. However, incorporating ceramics into polymer electrolytes can enhance lithium-ion conductivity and transference number. In our study, the sample containing 20 wt.% ceramic content (LTPO20) demonstrated a high lithium-ion transference number of ~ 0.71.

Inorganic lithium-ion conducting ceramic particles are known for their exceptionally high Li-ion transference number, often approaching 1. In the LTPO20 composite, the inclusion of LTPO ceramic particles constrains the transport of $(TFSI)^{-}$ and other poly-ions, thereby enhancing its Li-ion transference numbers relative to LTPO0, where t_{Li+} typically around 0.30. Additionally, the LTPO particles may function as Lewis acid sites, facilitating complexation between $(TFSI)^{-}$ and LTPO particles.[63] The LTPO20 electrolyte sample showed the highest conductivity along with the highest lithium-ion transference number among all the LTPOx samples. Considering the values of the lithium-ion transference number and the overall conductivity, the Li^{+} conductivity was calculated to be 0.63×10^{-4} S cm^{-1} for the LTPO20 sample.

3.6 Linear sweep voltammetry (LSV)

The linear sweep voltammetry profiles used to investigate the electrochemical stability window (ESW) of LTPO0 and LTPO20 samples are displayed in Figure 6(b). The higher voltage with a large change in current value represents the higher limit of the electrochemical stability window, within which the electrolyte maintains its electrochemical integrity during the charging-discharging of the cells. LSV was conducted on Li|LTPO0|SS and Li|LTPO20|SS cells in the 2.5 V to 6 V voltage range at a scan rate of 0.1 mV s^{-1}. The upper oxidation voltage value of LTPO0 was found to be 3.9 V, which was increased to 4.6 V upon incorporating LTPO ceramic filler in the LTPO20 solid electrolyte. A strong interaction between the ceramic fillers and the salted polymer chain enhanced the electrochemical stability of the PEO- P(VDF-HFP)-LiTFSI polymeric salt, which allows the application of high voltage cathode materials based on layered oxides, spinel structures.

3.7 Symmetric cell GCD

To investigate the interfacial stability between the LTPO20 membranes and the lithium metal, Li plating, and stripping tests were performed in a symmetric cell. Figure 7(a) displays the GCD curves of lithium symmetric cells with different current densities (0.2 mA cm^{-2}, 0.4 mA cm^{-2}, 0.6 mA cm^{-2}, 0.8 mA cm^{-2}, 1 mA cm^{-2}, and 1.5 mA cm^{-2}) for 30 minute periods of lithium plating and stripping.

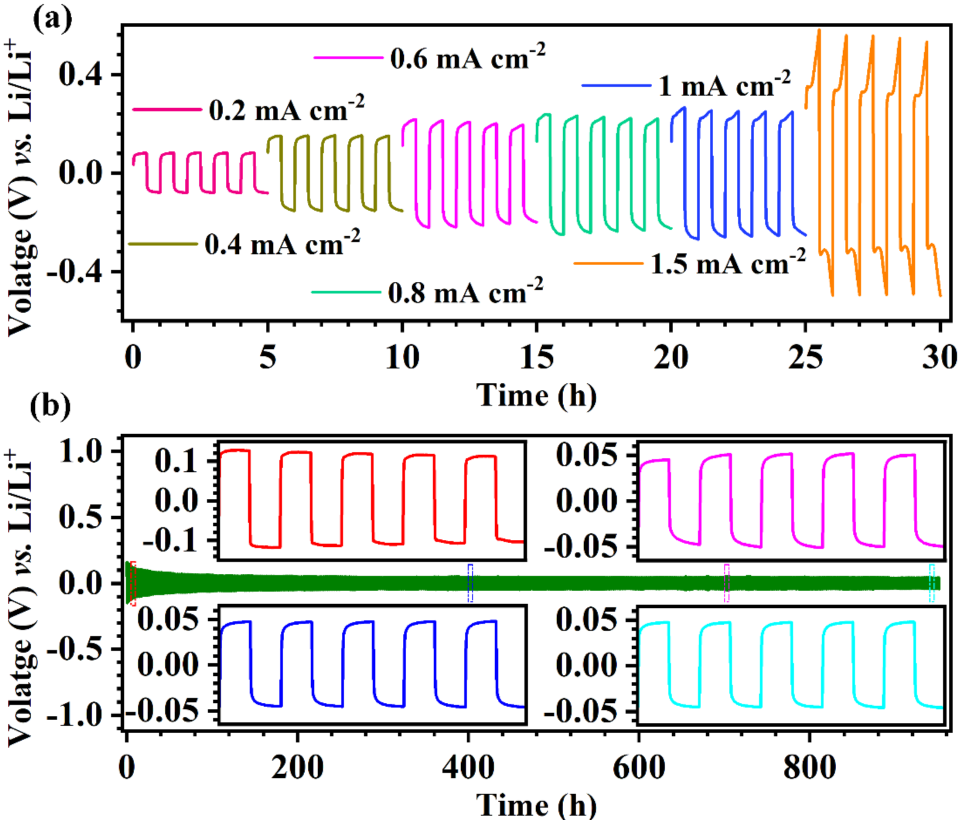

Figure 7: (a) The room temperature galvanostatic curves indicating lithium plating-stripping in Li|LTPO20|Li cells at different current densities. (b) The room temperature galvanostatic curves indicate lithium plating-stripping in Li|LTPO20|Li cell at a current of 0.2 mA cm^{-2} for 950 h.

As the current density increases to 1.5 mA cm^{-2}, the overpotential profile shows diminishing flatness and elevated potential values. At 1.5 mA cm^{-2}, indications of non-uniform lithium plating and stripping become apparent from the asymmetric voltage profile. Assessing the electrical integrity up to 1.5 mA cm^{-2}, the critical density of the LTPO20 electrolyte is estimated to be approximately 1 mA cm^{-2}. At the current density of 0.2 mA cm^{-2}, the lithium symmetric cell utilizing LTPO20 exhibits a flat over-potential of ~ 50 mV during plating and stripping, demonstrating durable cycling performance for 950 cycles without any sign of micro short-circuits or complete short circuits (Figure 7(b)). During the initial cycles, the over-potential decreases continuously until it reaches a constant value. The high over-potential in initial cycles could be attributed to the SEI formation and activation polarization. The nearly unchanged over-potential value over 950 cycles suggests the presence of a stable interface between the lithium metal electrode and composite electrolyte. Furthermore, the over-potential curve of the symmetric cell during plating and stripping indicates uniform lithium deposition and removal from the lithium metal surface.[64]

3.8 Full cell GCD

The Li|LTPO20|$LiFePO_4$ cell underwent galvanostatic charging and discharging under room temperature conditions, within a voltage window of 2.8-4.0 V. Figure 8(a) shows the specific capacity-potential curve for Li|LTPO20|$LiFePO_4$ at different C-rates. The cell delivered a specific capacity of ~ 141 mAh g^{-1} at 0.2C, which decreases to ~ 133 mAh g^{-1} and ~ 115 mAh g^{-1} at 0.5C and 1C, respectively (the C rate was calculated considering the specific capacity of $LiFePO_4$ as 160 mAh g^{-1}). The specific capacity degradation from 0.2C to 0.5C is lower than the reduction in specific capacity from 0.5C to 1C. This might be due to the sluggish lithium-ion transport kinetics at the electrode-electrolyte interface and the poor lithium-ion conductivity of $LiFePO_4$.[65, 66] Figure 8(b) showcases the long-term cyclability of Li|LTPO20|$LiFePO_4$ at 1C. The cell retained ~ 85% of the initial specific capacity after 500 charge-discharge cycles. The columbic efficiency remained nearly 100%, even with slight capacity degradations after every cycle. Figure 8(c) illustrates the charge-discharge profiles of Li|LTPO20|$LiFePO_4$ cells at selected cycles. With cycling, a slight increase in the over-potential associated with capacity degradation can be observed. This could be attributed to the increased SEI layer and structural degradation of $LiFePO_4$ particles associated with continuous cycling.

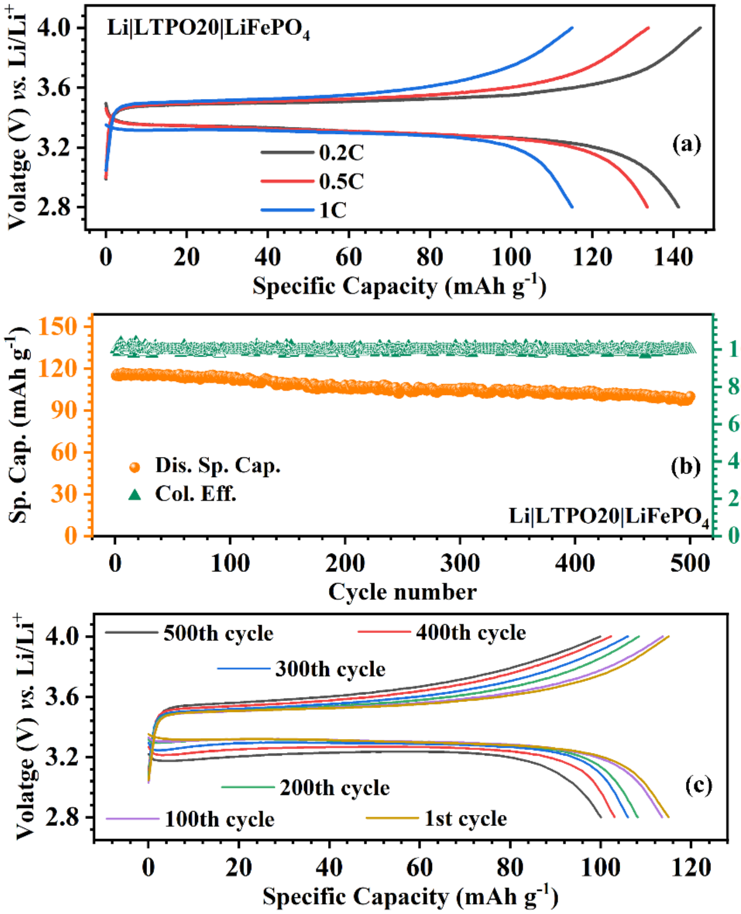

Figure 8: (a) The charge-discharge curves of Li|LTPO20|$LiFePO_4$ cell at different C-rates cycled at room temperature. (b) Room temperature long cycling data of Li|LTPO20|$LiFePO_4$ cell at 1C. (c) Galvanostatic charge-discharge curves of Li|LTPO20|$LiFePO_4$ cell at selected cycles.

4. Conclusions

The composite solid polymer electrolyte with 20 wt.% of high lithium-ion conducting $LiTa_2PO_8$ ceramic fillers exhibited the highest lithium-ion conductivity of 0.63×10^{-4} S cm^{-1} at room temperature along with the lowest activation energy value of ~ 0.25 eV among all LTPO*x* samples. The ceramic filler incorporation increased the oxidation stability of the LTPO0 polymer electrolyte from 3.9 V to 4.6 V for the LTPO20 composite sample against the lithium metal. The symmetric cell fabricated with LTPO20 as the electrolyte showed excellent uniform lithium plating-stripping at 0.2 mA cm^{-2} for 950 cycles. The critical current density estimated from Li plating-stripping tests was around 1 mA cm^{-2}. The Li|LTPO20|$LiFePO_4$ full cell delivered a high specific capacity of ~ 141 mAh g^{-1} at 0.2C and ~ 115 mAh g^{-1} at 1C. Furthermore, the cell retained 85% of its specific capacity after 500 cycles at 1C. The electrochemical performance driven by the LTPO20 composite solid electrolyte indicates the viability of LTPO-based composite electrolytes' application in lithium metal solid-state batteries.

SUPPORTING INFORMATION

Results of Rietveld refinement XRD data; XRD patterns of LTPO20 composite electrolyte and $LiTa_2PO_8$ ceramic sample; Nyquist plot of LTPO0, LTPO10, and LTPO30 electrolyte; Lithium-ion transference number (t_{Li+}) table

AUTHOR INFORMATION

Corresponding Author

Sunil Kumar

Department of Metallurgical Engineering and Materials Science, Indian Institute of Technology Indore, Simrol, 453552, India

Center for Electric Vehicle and Intelligent Transport Systems, Indian Institute of Technology Indore, Simrol, 453552, India; E-mail: sunil@iiti.ac.in

Authors

Asish Kumar Das – Department of Metallurgical Engineering and Materials Science, Indian Institute of Technology Indore, Simrol, 453552, India

Manish Badole – Department of Metallurgical Engineering and Materials Science, Indian Institute of Technology Indore, Simrol, 453552, India

Hari Narayanan Vasavan – Department of Metallurgical Engineering and Materials Science, Indian Institute of Technology Indore, Simrol, 453552, India

Samriddhi Saxena – Department of Metallurgical Engineering and Materials Science, Indian Institute of Technology Indore, Simrol, 453552, India

Pratiksha Gami – Department of Metallurgical Engineering and Materials Science, Indian Institute of Technology Indore, Simrol, 453552, India

Neha Dagar – Department of Metallurgical Engineering and Materials Science, Indian Institute of Technology Indore, Simrol, 453552, India

Author Contributions

The manuscript was written through the contributions of all authors. All authors have given approval to the final version of the manuscript.

Notes

The authors declare no competing financial interest.

DATA AVAILABILITY

Data will be made available on request.

ACKNOWLEDGMENTS

The author (AKD) thanks the Ministry of Education, Government of India, for the Prime Ministers Research Fellowship (PMRF) (PMRF ID - 2102737). The authors gratefully acknowledge the Science and Engineering Research Board (SERB), Government of India (Grant No. CRG/2021/005548) and Department of Science and Technology (DST), Government of India (Grant No. DST/TMD/IC-MAP/2K20/01).

References

1. Grey, C. P.; Hall, D. S., Prospects for lithium-ion batteries and beyond—a 2030 vision. *Nat. Commun.* **2020,** *11* (1), 6279.

2. Goodenough, J. B.; Park, K.-S., The Li-Ion Rechargeable Battery: A Perspective. *J. Am. Chem. Soc.* **2013,** *135* (4), 1167.

3. Albertus, P.; Anandan, V.; Ban, C.; Balsara, N.; Belharouak, I.; Buettner-Garrett, J.; Chen, Z.; Daniel, C.; Doeff, M.; Dudney, N. J.; Dunn, B.; Harris, S. J.; Herle, S.; Herbert, E.; Kalnaus, S.; Libera, J. A.; Lu, D.; Martin, S.; McCloskey, B. D.; McDowell, M. T.; Meng, Y. S.; Nanda, J.; Sakamoto, J.; Self, E. C.; Tepavcevic, S.; Wachsman, E.; Wang, C.; Westover, A. S.; Xiao, J.; Yersak, T., Challenges for and Pathways toward Li-Metal-Based All-Solid-State Batteries. *ACS Energy Lett.* **2021,** *6* (4), 1399.

4. Zhang, L.; Guo, H.; Zhang, Q.; Wang, A.; Su, Y.; Chen, Y.; Li, Y.; Shen, F.; Han, X., In Situ Formed Surface Layer to Improve the Air Stability of LLZTO and Its Contact with the Li Metal. *Energy Fuels* **2023,** *37* (18), 14341.

5. Alam, T.; Das, A., Review on Impurity and Conductivity Issues of Garnet Type $Li_7La_3Zr_2O_{12}$: Mechanisms, Solutions, and Perspectives. *Energy Fuels* **2023,** *37* (20), 15267.

6. Noh, H.; Kim, D.; Lee, W.; Jang, B.; Ha, J. S.; Yu, J. H., Surface Modification of Ga-Doped-LLZO ($Li_7La_3Zr_2O_{12}$) by the Addition of Polyacrylonitrile for the Electrochemical Stability of Composite Solid Electrolytes. *Energies* **2023,** *16* (23), 7695.

7. Samson, A. J.; Hofstetter, K.; Bag, S.; Thangadurai, V., A bird's-eye view of Li-stuffed garnet-type $Li_7La_3Zr_2O_{12}$ ceramic electrolytes for advanced all-solid-state Li batteries. *Energy Environ. Sci.* **2019,** *12* (10), 2957.

8. Inada, R.; Takeda, A.; Yamazaki, Y.; Miyake, S.; Sakurai, Y.; Thangadurai, V., Effect of Postannealing on the Properties of a Ta-Doped $Li_7La_3Zr_2O_{12}$Solid Electrolyte Degraded by Li Dendrite Penetration. *ACS Appl. Energy Mater.* **2020,** *3* (12), 12517.

9. Cheng, X.; Yan, Q.; Yan, R.; Pu, X.; Jiang, Y.; Huang, Y.; Zhu, X., Interfacial Modification of Ga-Substituted $Li_7La_3Zr_2O_{12}$ against Li Metal via a Simple Doping Method. *ACS Appl. Mater. Interfaces* **2023,** *15* (51), 59534.

10. Chen, H.; Cao, X.; Huang, M.; Ren, X.; Zhao, Y.; Yu, L.; Liu, Y.; Zhong, L.; Qiu, Y., In-situ interfacial passivation and self-adaptability synergistically stabilizing all-solid-state lithium metal batteries. *J. Energy Chem.* **2024,** *88*, 282.

11. Guo, Q.; Xu, F.; Shen, L.; Deng, S.; Wang, Z.; Li, M.; Yao, X., 20 μm-Thick $Li_{6.4}La_3Zr_{1.4}Ta_{0.6}O_{12}$-Based Flexible Solid Electrolytes for All-Solid-State Lithium Batteries. *Energy Mater. Adv.* **2022,** *2022*, 9753506.

12. Guo, Q.; Xu, F.; Shen, L.; Wang, Z.; Wang, J.; He, H.; Yao, X., Poly(ethylene glycol) brush on $Li_{6.4}La_3Zr_{1.4}Ta_{0.6}O_{12}$ towards intimate interfacial compatibility in composite polymer electrolyte for flexible all-solid-state lithium metal batteries. *J. Power Sources* **2021,** *498*, 229934.

13. Wan, Z.; Chen, X.; Zhou, Z.; Zhong, X.; Luo, X.; Xu, D., Atom substitution of the solid-state electrolyte $Li_{10}GeP_2S_{12}$ for stabilized all-solid-state lithium metal batteries. *J. Energy Chem.* **2024,** *88*, 28.

14. Yu, G.; Wang, Y.; Li, K.; Chen, D.; Qin, L.; Xu, H.; Chen, J.; Zhang, W.; Zhang, P.; Sun, Z., Solution-processable $Li_{10}GeP_2S_{12}$ solid electrolyte for a composite electrode in all-solid-state lithium batteries. *Sustain. Energy Fuels* **2021,** *5* (4), 1211.

15. Yan, H.; Yao, J.; Ye, Z.; Lin, Q.; Zhang, Z.; Li, S.; Song, D.; Wang, Z.; Yu, C.; Zhang, L., Al-F co-doping towards enhanced electrolyte-electrodes interface properties for halide and sulfide solid electrolytes. *Chin. Chem. Lett.* **2024**, 109568.

16. Song, R.; Yao, J.; Xu, R.; Li, Z.; Yan, X.; Yu, C.; Huang, Z.; Zhang, L., Metastable Decomposition Realizing Dendrite-Free Solid-State Li Metal Batteries. *Adv. Energy Mater.* **2023,** *13* (9), 2203631.

17. Buchberger, D. A.; Garbacz, P.; Słupczyński, K.; Brzezicki, A.; Boczar, M.; Czerwiński, A., Lithium Transport Studies on Chloride-Doped Argyrodites as Electrolytes for Solid-State Batteries. *ACS Appl. Mater. Interfaces* **2023,** *15* (46), 53417.

18. Taklu, B. W.; Nikodimos, Y.; Bezabh, H. K.; Lakshmanan, K.; Hagos, T. M.; Nigatu, T. A.; Merso, S. K.; Sung, H. Y.; Yang, S. C.; Wu, S. H.; Su, W. N.; Hwang, B. J., Air-stable iodized-oxychloride argyrodite sulfide and anionic swap on the practical potential window for all-solid-state lithium-metal batteries. *Nano Energy* **2023,** *112*, 108471.

19. Su, H.; Liu, Y.; Zhong, Y.; Li, J.; Wang, X.; Xia, X.; Gu, C.; Tu, J., Stabilizing the interphase between Li and Argyrodite electrolyte through synergistic phosphating process for all-solid-state lithium batteries. *Nano Energy* **2022,** *96*, 107104.

20. Liu, F.; Gao, L.; Zhang, Z.; Zhang, L.; Deng, N.; Zhao, Y.; Kang, W., Interfacial Challenges, processing strategies, and composite applications for high voltage all-solid-state

lithium batteries based on halide and sulfide solid-state electrolytes. *Energy Storage Mater.* **2024,** *64*, 103072.

21. Shi, Y.; Hu, L.; Li, Q.; Sun, Y.; Duan, Q.; Jiang, Y.; Xu, Y.; Yi, J.; Zhao, B.; Zhang, J., An optimizing hybrid interface architecture for unleashing the potential of sulfide-based all-solid-state battery. *Energy Storage Mater.* **2023,** *63*, 103009.

22. Pareek, T.; Dwivedi, S.; Singh, B.; Kumar, D.; Kumar, P.; Kumar, S., $LiSnZr(PO_4)_3$: NASICON-type solid electrolyte with excellent room temperature Li^+ conductivity. *J. Alloys Compd.* **2019,** *777*, 602.

23. Das, A. K.; Badole, M.; Vasavan, H. N.; Saxena, S.; Gami, P.; Kumar, S., Highly conductive ceramic-in-polymer composite electrolyte enabling superior electrochemical performance for all-solid-state lithium batteries. *Ceram. Int.* **2023,** *49* (18), 29719.

24. Yu, X.; Manthiram, A., A review of composite polymer-ceramic electrolytes for lithium batteries. *Energy Storage Mater.* **2021,** *34*, 282.

25. Fenton, D. E.; Parker, J. M.; Wright, P. V., Complexes of alkali metal ions with poly(ethylene oxide). *Polymer* **1973,** *14* (11), 589.

26. Wang, Z.; Huang, B.; Huang, H.; Chen, L.; Xue, R.; Wang, F., Investigation of the position of Li^+ ions in a polyacrylonitrile-based electrolyte by Raman and infrared spectroscopy. *Electrochim. Acta* **1996,** *41* (9), 1443.

27. Tominaga, Y.; Yamazaki, K.; Nanthana, V., Effect of Anions on Lithium Ion Conduction in Poly(ethylene carbonate)-based Polymer Electrolytes. *J. Electrochem. Soc.* **2015,** *162* (2), A3133.

28. Sukeshini, A. M.; Nishimoto, A.; Watanabe, M., Transport and electrochemical characterization of plasticized poly(vinyl chloride) solid electrolytes. *Solid State Ion.* **1996,** *86-88* (PART 1), 385.

29. Saikia, D.; Wu, H.-Y.; Pan, Y.-C.; Lin, C.-P.; Huang, K.-P.; Chen, K.-N.; Fey, G. T. K.; Kao, H.-M., Highly conductive and electrochemically stable plasticized blend polymer electrolytes based on PVdF-HFP and triblock copolymer PPG-PEG-PPG diamine for Li-ion batteries. *J. Power Sources* **2011,** *196* (5), 2826.

30. Grewal, M. S.; Tanaka, M.; Kawakami, H., Free-standing polydimethylsiloxane-based cross-linked network solid polymer electrolytes for future lithium ion battery applications. *Electrochim. Acta* **2019,** *307*, 148.

31. Song, Z.; Chen, F.; Martinez-Ibañez, M.; Feng, W.; Forsyth, M.; Zhou, Z.; Armand, M.; Zhang, H., A reflection on polymer electrolytes for solid-state lithium metal batteries. *Nat. Commun.* **2023,** *14* (1), 4884.

32. Wang, Z.; Shen, L.; Deng, S.; Cui, P.; Yao, X., 10 μm-Thick High-Strength Solid Polymer Electrolytes with Excellent Interface Compatibility for Flexible All-Solid-State Lithium-Metal Batteries. *Adv. Mater.* **2021,** *33* (25), 2100353.

33. Wang, J.; Yang, J.; Shen, L.; Guo, Q.; He, H.; Yao, X., Synergistic Effects of Plasticizer and 3D Framework toward High-Performance Solid Polymer Electrolyte for Room-Temperature Solid-State Lithium Batteries. *ACS Appl. Energy Mater.* **2021,** *4* (4), 4129.

34. Wang, Z.; Guo, Q.; Jiang, R.; Deng, S.; Ma, J.; Cui, P.; Yao, X., Porous poly(vinylidene fluoride) supported three-dimensional poly(ethylene glycol) thin solid polymer electrolyte for flexible high temperature all-solid-state lithium metal batteries. *Chem. Eng. J.* **2022,** *435*, 135106.

35. Yu, J.; Kwok, S. C. T.; Lu, Z.; Effat, M. B.; Lyu, Y.-Q.; Yuen, M. M. F.; Ciucci, F., A Ceramic-PVDF Composite Membrane with Modified Interfaces as an Ion-Conducting Electrolyte for Solid-State Lithium-Ion Batteries Operating at Room Temperature. *ChemElectroChem* **2018,** *5* (19), 2873.

36. Yu, J.; Lyu, Y.-Q.; Liu, J.; Effat, M. B.; Kwok, S. C. T.; Wu, J.; Ciucci, F., Enabling non-flammable Li-metal batteries via electrolyte functionalization and interface engineering. *J. Mater. Chem. A* **2019,** *7* (30), 17995.

37. Dai, Z.; Yu, J.; Liu, J.; Liu, R.; Sun, Q.; Chen, D.; Ciucci, F., Highly conductive and nonflammable composite polymer electrolytes for rechargeable quasi-solid-state Li-metal batteries. *J. Power Sources* **2020,** *464*, 228182.

38. Sreejith, O. V.; Elsin Abraham, S.; Ramaswamy, M., Free-Standing and Flexible Garnet-PVDF Ceramic Polymer Electrolyte Membranes for Solid-State Batteries. *Energy Fuels* **2023,** *37* (3), 2401.

39. Panneerselvam, T.; Murugan, R.; Sreejith, O. V.; Moulisvar, M.; Elsin Abraham, S., 3D Flexible Electrospun Nanocomposite Polymer Electrolyte Based on $Li_{1.45}Al_{0.45}Ge_{0.2}Ti_{1.35}(PO_4)_3$ for Lithium Metal Batteries. *Energy Fuels* **2024,** *38* (1), 682.

40. Das, A. K.; Badole, M.; Vasavan, H. N.; Saxena, S.; Gami, P.; Deswal, S.; Kumar, P.; Kumar, S., Enhancing room temperature performance of solid-state lithium cell via a facile solid electrolyte-cathode interface design. *Mater. Today Sustain.* **2024,** *26*, 100758.

41. Luo, B.; Wang, W.; Wang, Q.; Ji, W.; Yu, G.; Liu, Z.; Zhao, Z.; Wang, X.; Wang, S.; Zhang, J., Facilitating ionic conductivity and interfacial stability via oxygen vacancies-enriched TiO_2 microrods for composite polymer electrolytes. *Chem. Eng. J.* **2023,** *460*, 141329.

42. Khan, K.; Fu, B.; Xin, H.; Beshiwork, B. A.; Hanif, M. B.; Wu, J.; Fang, Z.; Yang, J.; Li, T.; Chen, C.; Motola, M.; Xu, Z.; Wu, M., Composite polymer electrolyte incorporating WO_3 nanofillers with enhanced performance for dendrite-free solid-state lithium battery. *Ceram. Int.* **2023,** *49* (3), 4473.

43. Yang, T.; Zheng, J.; Cheng, Q.; Hu, Y.-Y.; Chan, C. K., Composite Polymer Electrolytes with $Li_7La_3Zr_2O_{12}$ Garnet-Type Nanowires as Ceramic Fillers: Mechanism of Conductivity Enhancement and Role of Doping and Morphology. *ACS Appl. Mater. Interfaces* **2017,** *9* (26), 21773.

44. Kim, J.; Kim, J.; Avdeev, M.; Yun, H.; Kim, S.-J., $LiTa_2PO_8$: a fast lithium-ion conductor with new framework structure. *J. Mater. Chem. A* **2018,** *6* (45), 22478.

45. Dai, R.; Avdeev, M.; Kim, S.-J.; Prasada Rao, R.; Adams, S., Temperature Dependence of Structure and Ionic Conductivity of $LiTa_2PO_8$ Ceramics. *Chem. Mater.* **2022,** *34* (23), 10572.

46. Coelho, A., TOPAS and TOPAS-Academic: an optimization program integrating computer algebra and crystallographic objects written in C++. *J. Appl. Crystallogr.* **2018,** *51* (1), 210.

47. Momma, K.; Izumi, F., VESTA: a three-dimensional visualization system for electronic and structural analysis. *J. Appl. Crystallogr.* **2008,** *41* (3), 653.

48. Wong, L. L.; Phuah, K. C.; Dai, R.; Chen, H.; Chew, W. S.; Adams, S., Bond Valence Pathway Analyzer—An Automatic Rapid Screening Tool for Fast Ion Conductors within softBV. *Chem. Mater.* **2021,** *33* (2), 625.

49. Chen, H.; Wong, L. L.; Adams, S., SoftBV - a software tool for screening the materials genome of inorganic fast ion conductors. *Acta. Crystallogr. B.* **2019,** *75* (1), 18.

50. Seol, J.-c.; Balasubramaniam, R.; Aravindan, V.; Thangavel, R.; Lee, Y.-S., Ameliorating the electrode/electrolyte interface compatibility in Li-ion solid-state batteries with plasticizer. *J. Alloys Compd.* **2022,** *927*, 167077.

51. Tripathi, M.; Bobade, S. M.; Kumar, A., Preparation of polyvinylidene fluoride-co-hexafluoropropylene-based polymer gel electrolyte and its performance evaluation for application in EDLCs. *Bull. Mater. Sci.* **2019,** *42* (1), 27.

52. M. Shanthi, P.; J. Hanumantha, P.; Albuquerque, T.; Gattu, B.; Kumta, P. N., Novel Composite Polymer Electrolytes of PVdF-HFP Derived by Electrospinning with Enhanced Li-Ion Conductivities for Rechargeable Lithium–Sulfur Batteries. *ACS Appl. Energy Mater.* **2018,** *1* (2), 483.

53. Wieczorek, W.; Raducha, D.; Zalewska, A.; Stevens, J. R., Effect of Salt Concentration on the Conductivity of PEO-Based Composite Polymeric Electrolytes. *J. Phys. Chem. B* **1998,** *102* (44), 8725.

54. Brouillette, D.; Irish, D. E.; Taylor, N. J.; Perron, G.; Odziemkowski, M.; Desnoyers, J. E., Stable solvates in solution of lithium bis(trifluoromethylsulfone)imide in glymes and other aprotic solvents: Phase diagrams, crystallography and Raman spectroscopy. *Phys. Chem. Chem. Phys.* **2002,** *4* (24), 6063.

55. Wang, Z.; Gao, W.; Huang, X.; Mo, Y.; Chen, L., Spectroscopic studies on interactions and microstructures in propylene carbonate - LiTFSI electrolytes. *J. Raman Spectrosc.* **2001,** *32* (11), 900.

56. Sheng, O.; Jin, C.; Luo, J.; Yuan, H.; Huang, H.; Gan, Y.; Zhang, J.; Xia, Y.; Liang, C.; Zhang, W.; Tao, X., $Mg_2B_2O_5$ Nanowire Enabled Multifunctional Solid-State Electrolytes with High Ionic Conductivity, Excellent Mechanical Properties, and Flame-Retardant Performance. *Nano Lett.* **2018,** *18* (5), 3104.

57. Yu, J.; Zhou, G.; Li, Y.; Wang, Y.; Chen, D.; Ciucci, F., Improving Room-Temperature Li-Metal Battery Performance by In Situ Creation of Fast Li^+ Transport Pathways in a Polymer-Ceramic Electrolyte. *Small* **2023,** *19* (39), 2302691.

58. Wei, B.; Li, Y.; Lin, W.; Yu, J.; Chen, D., A wrapped and infiltrated ~20-μm-thick 3D ceramic framework composite enables fast Li^+ diffusion and interfacial compatibility for lithium-metal batteries. *Compos. B Eng.* **2024,** *272*, 111192.

59. Callegari, D.; Bonizzoni, S.; Berbenni, V.; Quartarone, E.; Mustarelli, P., Is It Possible to Obtain Solvent-Free, Li^+-Conducting Solid Electrolytes Based on Pure PVdF? Comment on “Self-Suppression of Lithium Dendrite in All-Solid-State Lithium Metal Batteries with Poly(vinylidene difluoride)-Based Solid Electrolytes”. *Adv. Mater.* **2020,** *32* (14), 1907375.

60. Zhang, X.; Wang, S.; Xue, C.; Xin, C.; Lin, Y.; Shen, Y.; Li, L.; Nan, C.-W., Response to Comment on "Self-Suppression of Lithium Dendrite in All-Solid-State Lithium Metal Batteries with Poly(vinylidene difluoride)-Based Solid Electrolytes". *Adv. Mater.* **2020,** *32* (14), 2000026.

61. Zhang, X.; Wang, S.; Xue, C.; Xin, C.; Lin, Y.; Shen, Y.; Li, L.; Nan, C.-W., Self-Suppression of Lithium Dendrite in All-Solid-State Lithium Metal Batteries with Poly(vinylidene difluoride)-Based Solid Electrolytes. *Adv. Mater.* **2019,** *31* (11), 1806082.

62. Evans, J.; Vincent, C. A.; Bruce, P. G., Electrochemical measurement of transference numbers in polymer electrolytes. *Polymer* **1987,** *28* (13), 2324.

63. Li, Z.; Huang, H.-M.; Zhu, J.-K.; Wu, J.-F.; Yang, H.; Wei, L.; Guo, X., Ionic Conduction in Composite Polymer Electrolytes: Case of PEO:Ga-LLZO Composites. *ACS Appl. Mater. Interfaces* **2019,** *11* (1), 784.

64. He, X.; Yang, Y.; Cristian, M. S.; Wang, J.; Hou, X.; Yan, B.; Li, J.; Zhang, T.; Paillard, E.; Swietoslawski, M.; Kostecki, R.; Winter, M.; Li, J., Uniform lithium electrodeposition for stable lithium-metal batteries. *Nano Energy* **2020,** *67*, 104172.

65. Wang, C.; Hong, J., Ionic/electronic conducting characteristics of $LiFePO_4$ cathode materials. *Electrochem. Solid-State Lett.* **2007,** *10* (3), A65.

66. Jiao, L. X.; Li, Z. Q.; Zhu, Y. Z.; Wei, Z.; Liang, Y.; Wang, X. L.; Cui, Y.; Zhang, Z. H.; He, M.; Song, B., Enhanced electrical conductivity and lithium ion diffusion rate of $LiFePO_4$ by Fe site and P site doping. *AIP Adv.* **2023,** *13* (7), 2158.

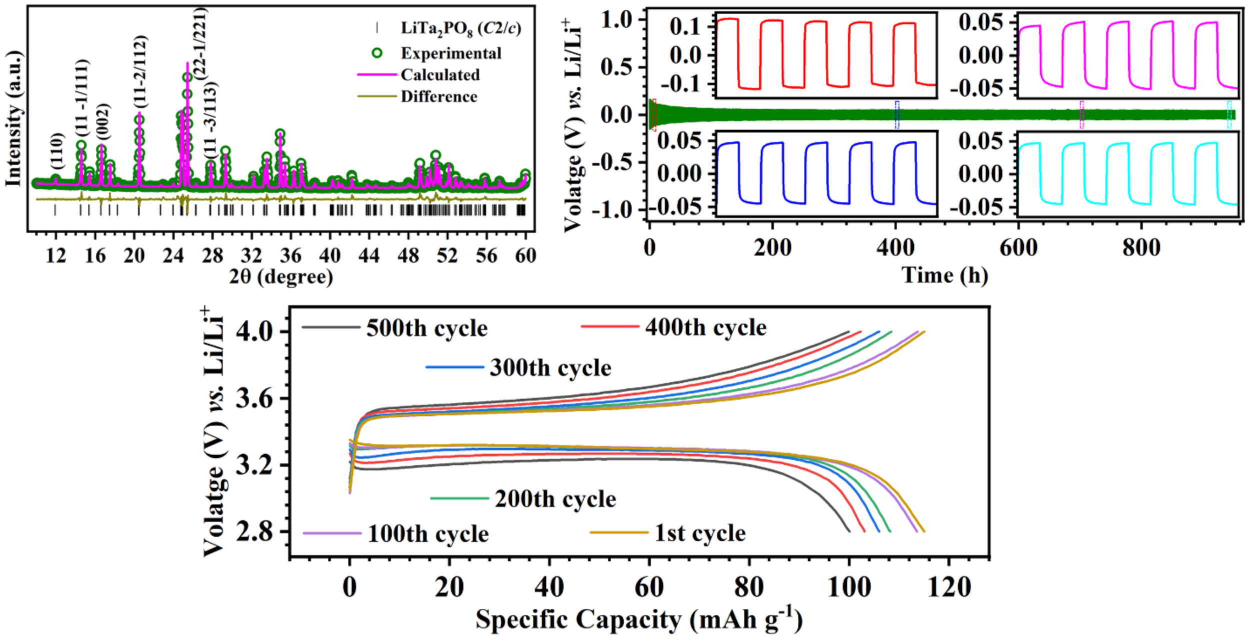
LiTa$_2$PO$_8$ (C2/c)
Experimental
Calculated
Difference
(110)
(11 -1/111)
(002)
(11-2/112)
(22-1/221)
(11 -3/113)
Intensity (a.u.)
2θ (degree)
12
16
20
24
28
32
36
40
44
48
52
56
60
Volatge (V) vs. Li/Li$^+$
Time (h)
1.0
0.5
0.0
-0.5
-1.0
0
200
400
600
800
0.1
0.0
-0.1
0.05
0.00
-0.05
500th cycle
400th cycle
300th cycle
200th cycle
100th cycle
1st cycle
Volatge (V) vs. Li/Li$^+$
4.0
3.6
3.2
2.8
Specific Capacity (mAh g^{-1})
0
20
40
60
80
100
120

TOC

[Supporting Information]

$LiTa_2PO_8$-based Polymer-Ceramic Electrolyte Paved the way to High-Performance Solid-State Lithium Metal Batteries

Asish Kumar Das[a], Manish Badole[a], Hari Narayanan Vasavan[a], Samriddhi Saxena[a], Pratiksha Gami[a],

Neha Dagar[a], Sunil Kumar [a,b,]*

[a]Department of Metallurgical Engineering and Materials Science, Indian Institute of Technology Indore, Simrol,

453552, India

[b]Center for Electric Vehicle and Intelligent Transport Systems, Indian Institute of Technology Indore, Simrol,

453552, India

*Corresponding author E-mail: sunil@iiti.ac.in

Table S1: Results of Rietveld refinement of room temperature powder XRD data of LTPO ($LiTa_2PO_8$) ceramics.

Site	**Site symmetry**	**x**	**y**	**z**	**Atom**	**Occupancy**
Ta1	8	0.2446	0.0948	0.2542	Ta^{+5}	1
Ta2	4	0	0.3462	0.25	Ta^{+5}	1
Ta3	4	0	0	0	Ta^{+5}	1
P	8	0.4996	0.2101	0.0594	P^{+4}	0.775
O1	8	0.0587	0.3325	0.0681	O^{-2}	1
O2	8	0.3797	0.1345	0.4057	O^{-2}	1
O3	8	0.3574	0.5055	0.1299	O^{-2}	1
O4	8	0.0464	0.1641	0.5519	O^{-2}	1
O5	8	0.1447	0.2374	0.2897	O^{-2}	1
O6	8	0.1387	0.058	0.1135	O^{-2}	1
O7	8	0.3785	0.2009	0.1538	O^{-2}	1
O8	8	0.1346	0.4655	0.2836	O^{-2}	1
Li1	8	0.759	0.154	0.653	Li^{+1}	0.41
Li2	8	0.236	0.359	0.418	Li^{+1}	0.31
Li3	8	0.166	0.525	0.498	Li^{+1}	0.23
Li4	8	0.347	0.351	0.257	Li^{+1}	0.05

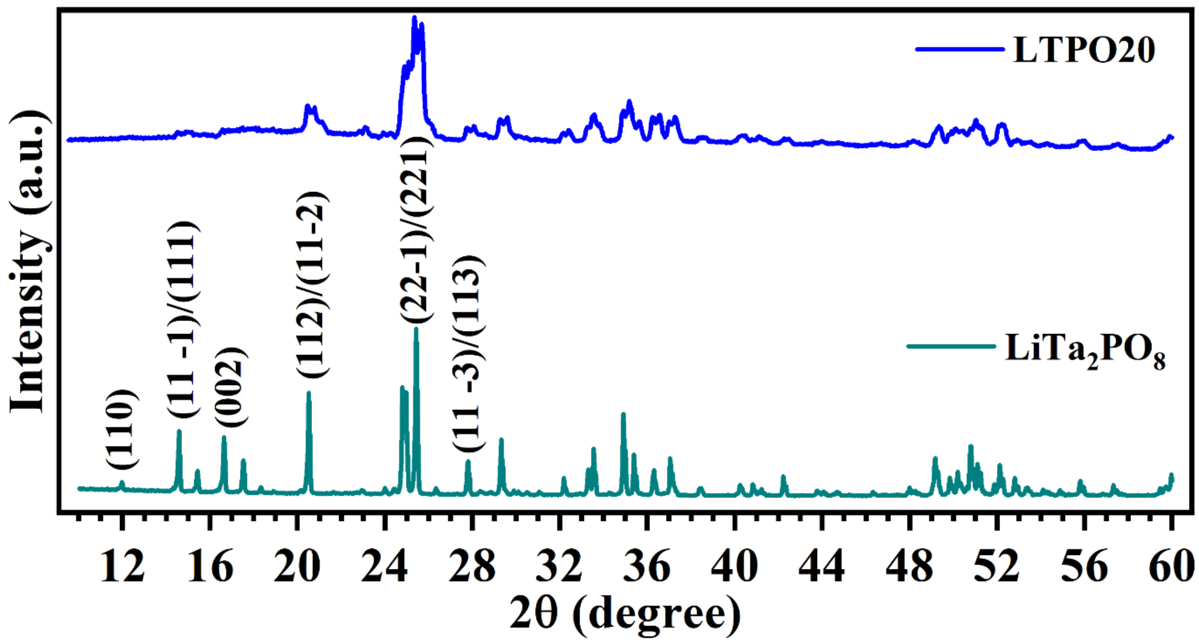

Figure S3: Room temperature XRD patterns of LTPO20 composite electrolyte and $LiTa_2PO_8$ ceramic sample.

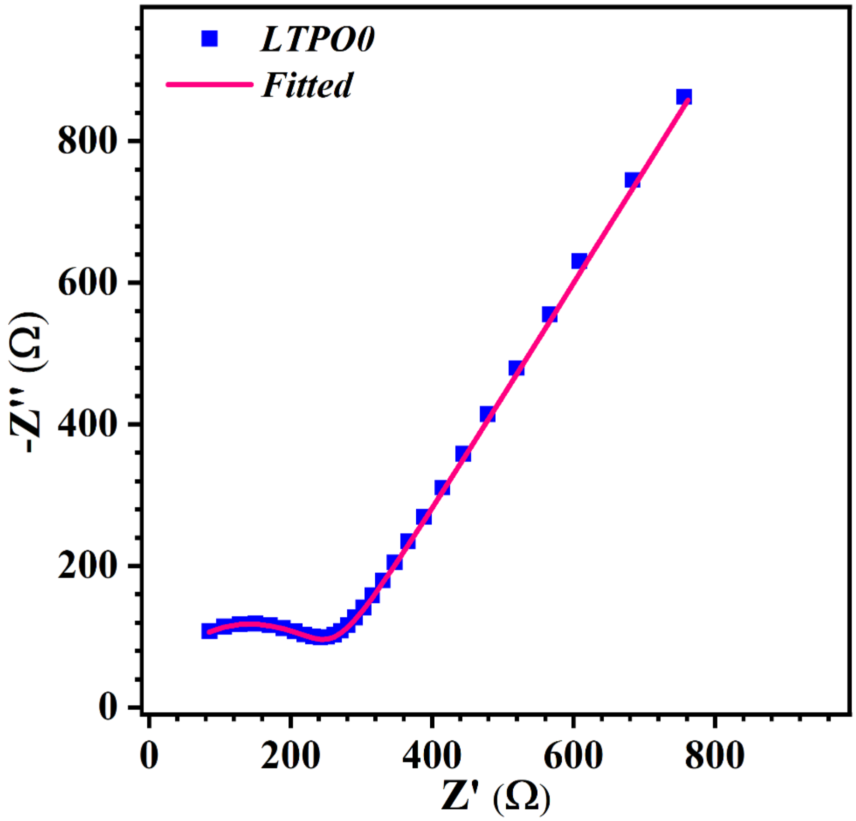

Figure S4: Nyquist plot of LTPO0 electrolyte.

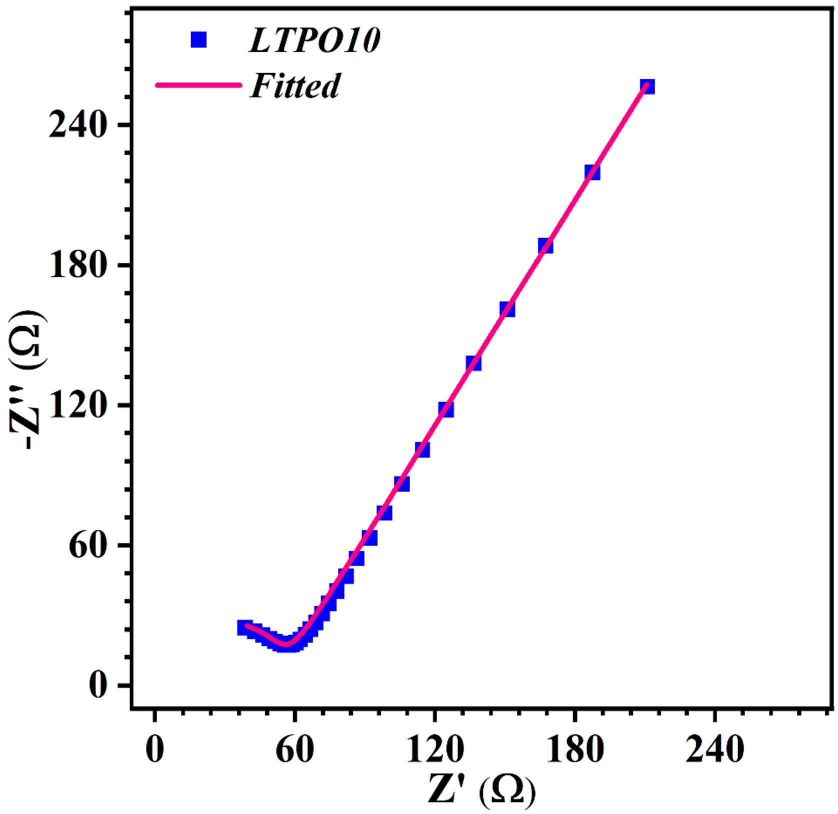

Figure S5: Nyquist plot of LTPO10 electrolyte.

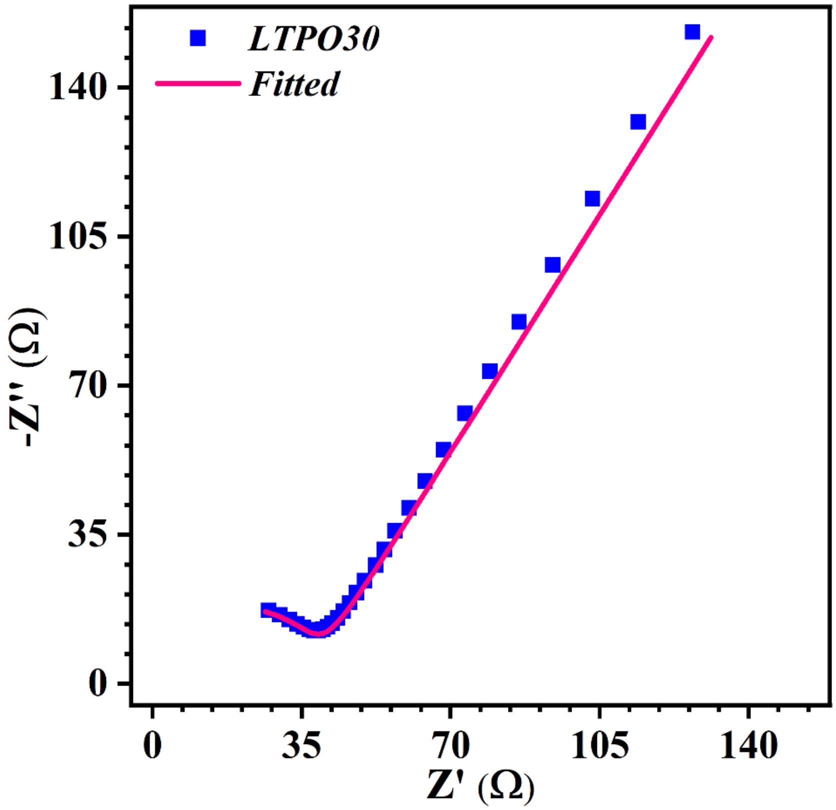

Figure S6: Nyquist plot of LTPO30 electrolyte.

Table S2: Lithium-ion transference number (t_{Li^+}) calculated for LTPO0, LTPO10, LTPO20, and LTPO30 (applied DC voltage = 0.05 V).

Sample	I_0 **(µA)**	I_{ss} **(µA)**	R_0 **(Ω)**	R_{ss} **(Ω)**	t_{Li^+}
LTPO0	96	45	170	220	0.39(3)
LTPO10	82	51	140	170	0.57(9)
LTPO20	180	140	90	95	0.71(6)
LTPO30	46	32	120	130	0.67(5)